# Solar-light driven h-$WO_3$/2H-$WS_2$-microalgae derived photocatalyst for rapid multi-dye degradation

Shrinath Bhat [a, c], U. T. Uthappa [b*], Shervin Kabiri [c], Heon-Ho Jeong [d*] and Mahaveer D. Kurkuri [a*]

[a] Centre for Research in Functional Materials (CRFM), JAIN (Deemed-to-be University), Jain Global Campus, Bengaluru-562112, Karnataka, India

[b] College of Chemistry and Environmental Engineering, Shenzhen University, Shenzhen 518055, China

[c] Adelaide University, School of Agriculture, Food and Wine, Waite Campus, Urrbrae, SA 5064, Australia

[d] Department of Chemical and Biomolecular Engineering, Chonnam National University, 50 Daehak-ro, Yeosu, Jeollanam-do 59626, Republic of Korea

[*] Corresponding authors.

E-mail address: sanjuuthappa@gmail.com, jeonghh29@jnu.ac.kr & mahaveer.kurkuri@jainuniversity.ac.in.

## 1. Characterization:

The surface chemistry of DE, $WS_xO_y$ and DE-$WS_xO_y$ were analyzed via the PerkinElmer FTIR instrument by the KBr pellet method, and the analysis was done in the range of 4000-500 $cm^{-1}$. Brunauer Emmett and Teller (BET) analysis was carried out to determine the multipoint surface area and Barrett-Joyner-Halenda (BJH) studies were done to calculate the total pore volume. Adsorption-desorption studies were carried out by using $N_2$ at liquid nitrogen temperature (-196 $^oC$) on Belsorp-Max (M/s. Microtarc BEL, Japan). To explore the structural features of the catalysts, Powder X-ray diffraction (XRD) patterns for the samples were recorded on an Ultima-IV X-ray diffractometer (M/s. Rigaku Corporation, Japan) Ni filtered Cu Kα radiations (1=1.5406 $A^o$) with a 2θ scan speed of 2 degrees/min and a scan range of 5 to 80 degrees at 40 kV and 30 Ma. The surface morphological features of the prepared DE, $WS_xO_y$ and DE-$WS_xO_y$ were observed by Jeol JSM-7100F Field-Emission Scanning Electron Microscopy (FESEM). The surface charges of the DE, $WS_xO_y$ and DE-$WS_xO_y$ were measured by Litesizer 500 (Anton Paar) zeta potential instrument in an aqueous solution using Omega Cuvete Z. The state of elements and elemental composition in the samples (DE, $WS_xO_y$ and

DE-$WS_xO_y$) were analysed by X-ray Photoelectron Spectroscopy (XPS; Thermo Scientific K-Alpha system and Al K-alpha X-ray source and an ion source energy range of 100 V to 3 KeV). Further, the thermal stability of the materials was evaluated from thermal gravimetric analysis (TGA) by PerkinElmer Diamond TG/DTA at a heating rate of 10 °C in an $N_2$ atmosphere. Photoluminescence (PL) Spectroscopy (Edinburgh instruments, FLS 1000; Detector R928P visible, Lamp-Xenon) was used to acquire PL spectra under identical settings and background-subtracted; inner-filter correction and integration window used for quantitative analysis. Metal ion analysis was carried out through Inductively Coupled Plasma - Optical Emission Spectroscopy (PerkinElmer Avio$^{TM}$ 200).

## 2. EDXS Elemental Mapping:

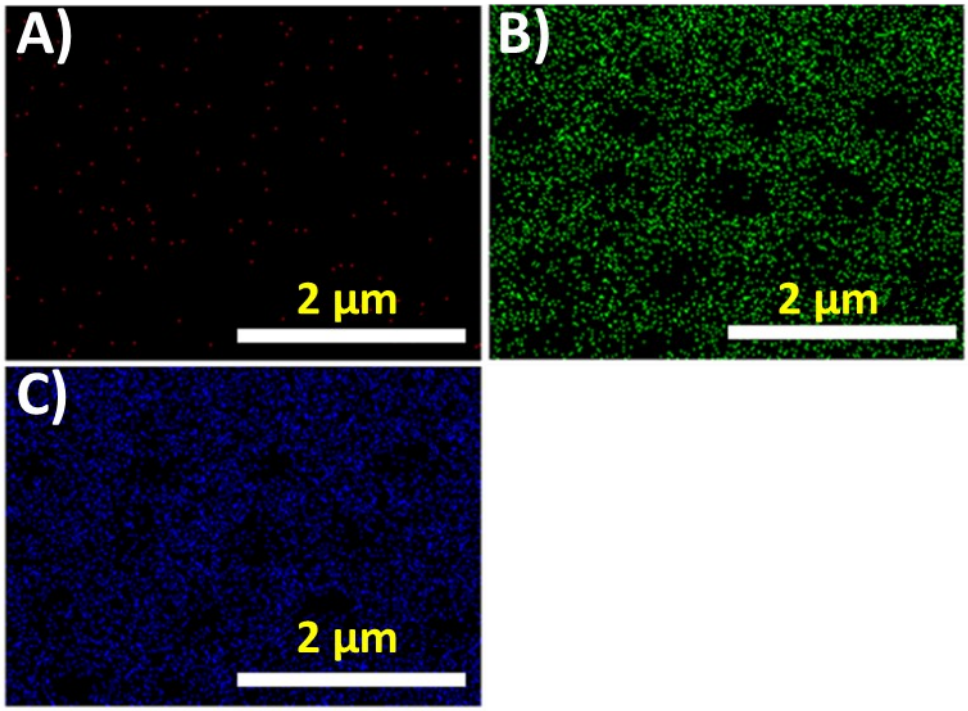


**Figure S1:** EDXS elemental mapping of A) C, B) O, C) Si elements for DE.

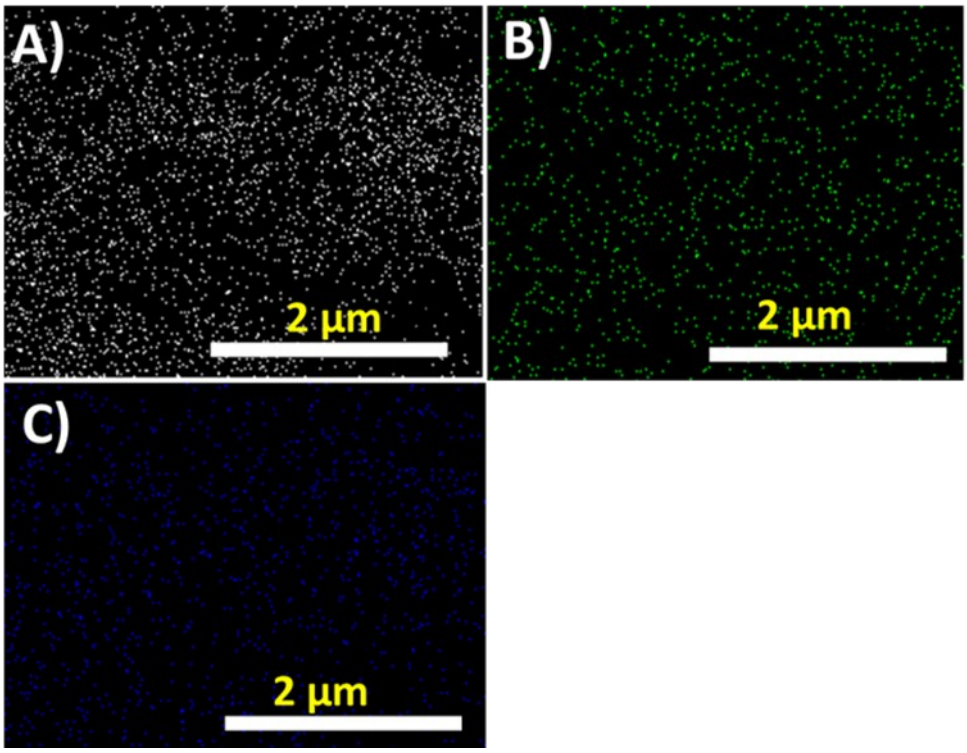


**Figure S2:** EDXS elemental mapping of A) O, B) W, C) S elements for $WS_xO_y$.

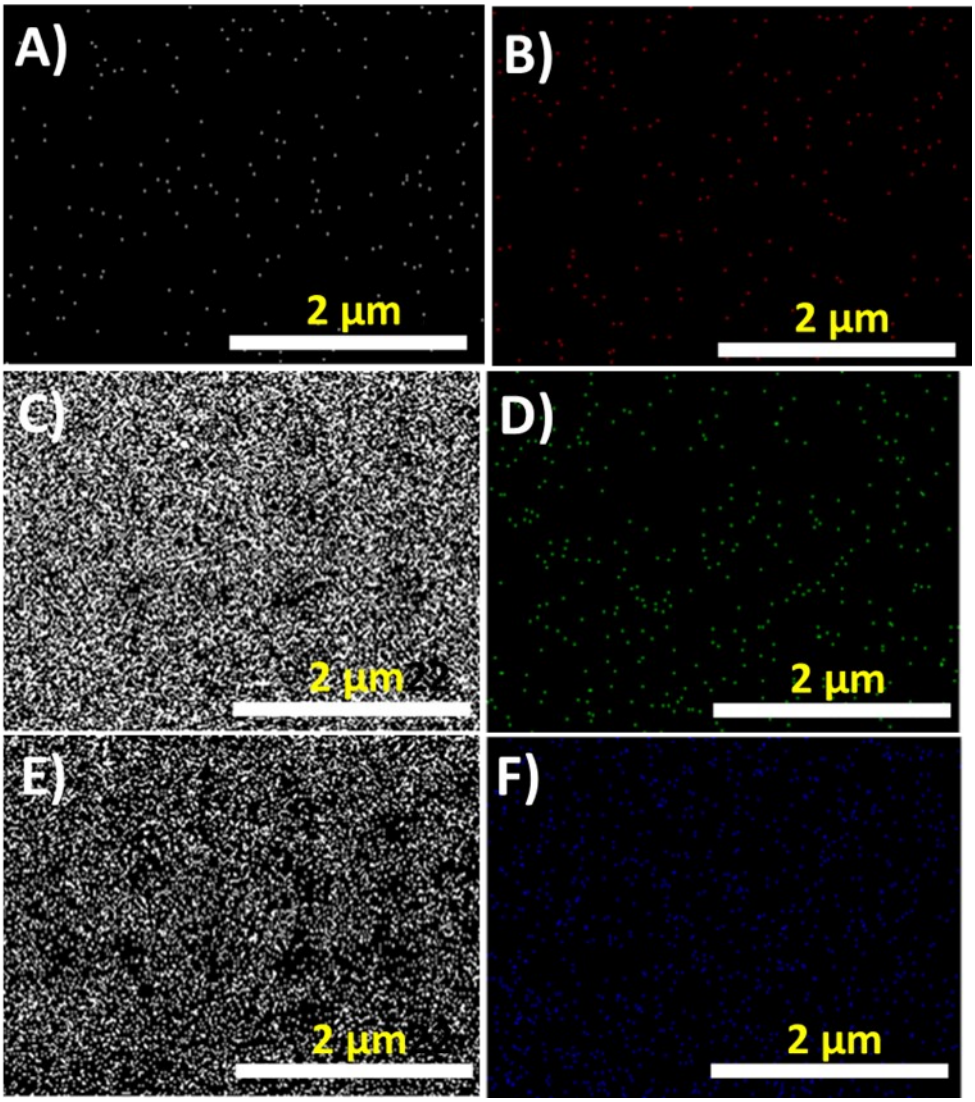


**Figure S3:** EDXS elemental mapping of A) C, B) N, C) Si, D) W, E) O, F) S elements for DE-$WS_xO_y$.

## 3. EDAX Spectra:

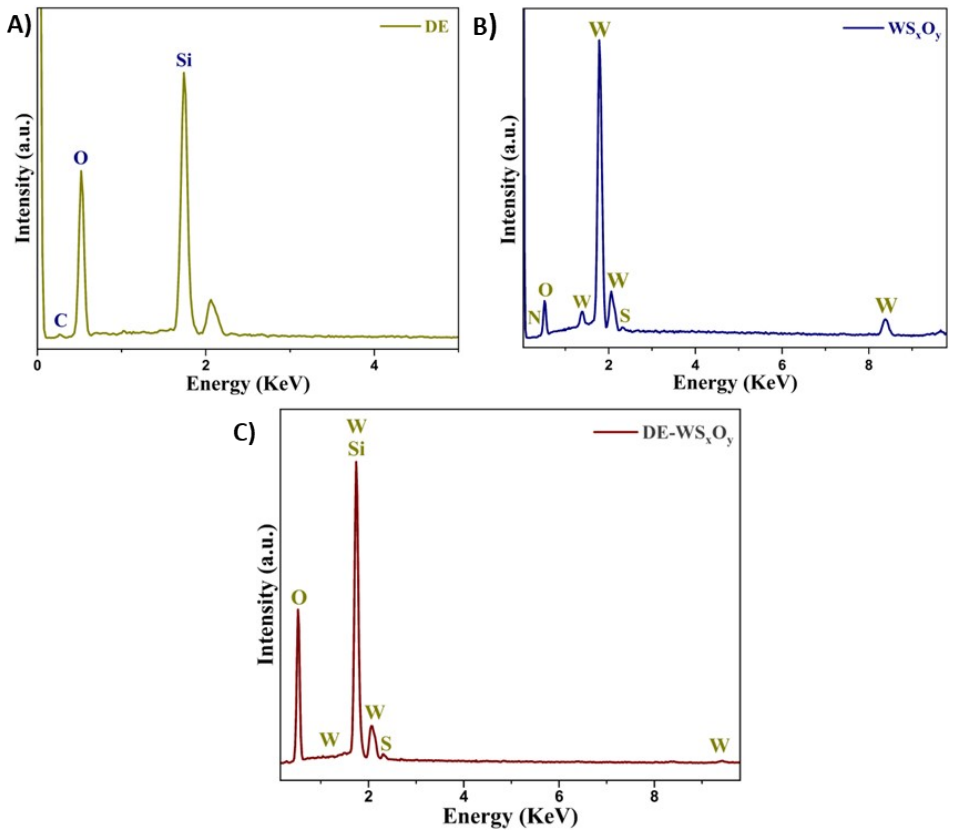


**Figure S4:** The energy dispersive X-ray analysis (EDAX) spectra of A) DE, B) $WS_xO_y$ and C) DE-$WS_xO_y$.

4. **EDS Elemental Mapping Images (TEM):**

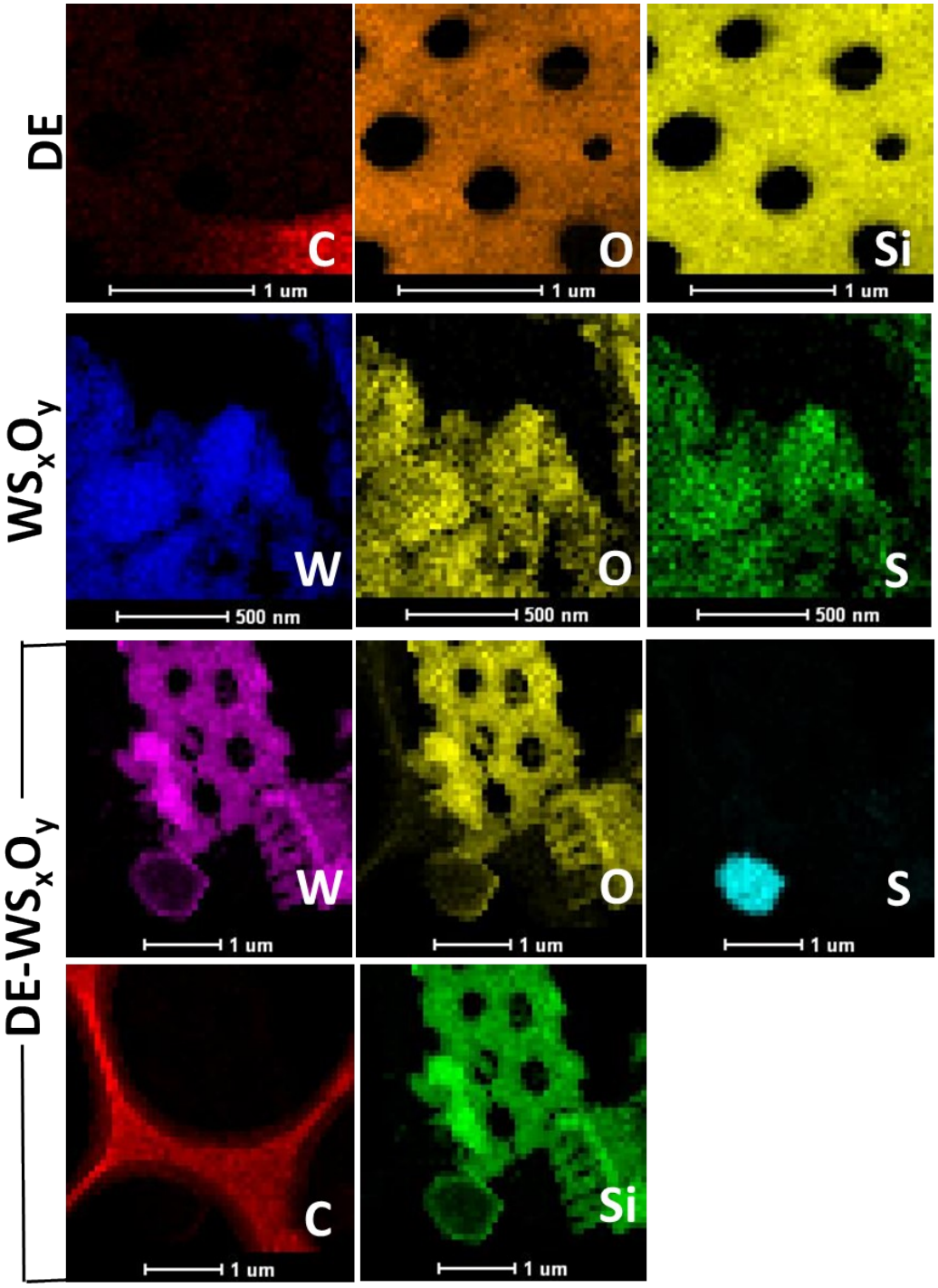


**Figure S5:** The energy dispersive X-ray spectroscopy (EDS) elemental mapping images.

## 5. FE-SEM Images:

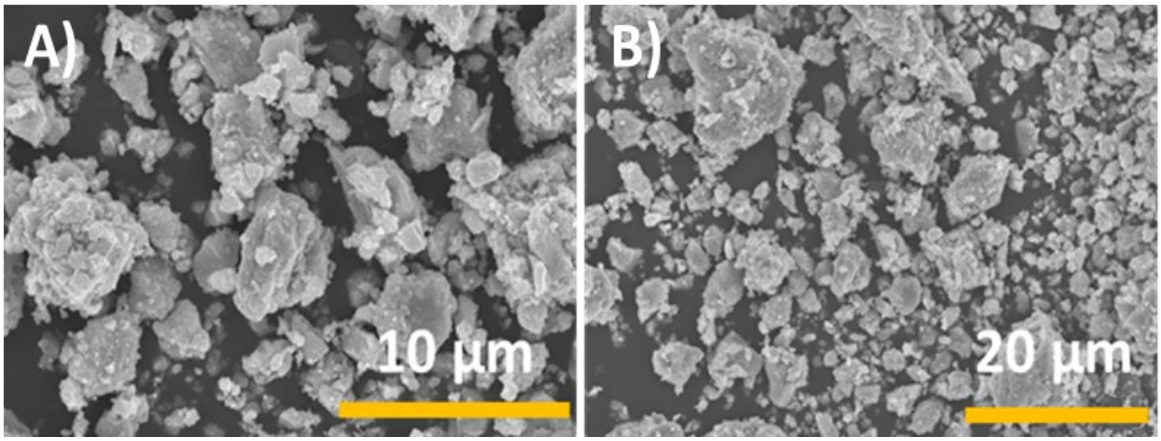


**Figure S6:** FE-SEM images for $WS_xO_y$.

## 6. TEM Images and Analysis:

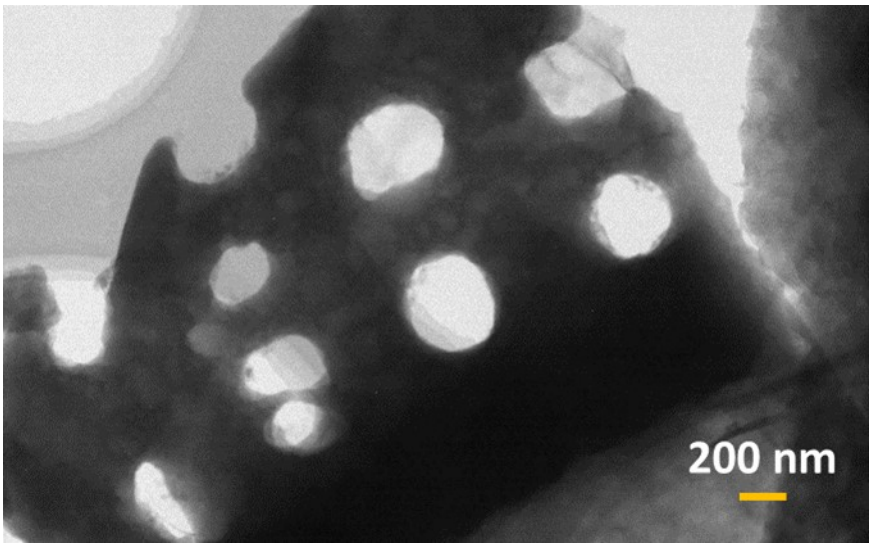


**Figure S7:** TEM images for DE frustule.

**Table S1:** Calculation of Miller indices for $WS_xO_y$.

| S.No. | 1/2r ($nm^{-1}$) | 1/r ($nm^{-1}$) | r (nm) | d-spacing ($A^o$) | (hkl) |
|---|---|---|---|---|---|
| 1 | 5.574446 | 2.787223 | 0.35878 | 3.587801 | (1 0 0) |
| 2 | 6.383706 | 3.191853 | 0.313298 | 3.132976 | (2 0 0) |
| 3 | 8.272085 | 4.136043 | 0.241777 | 2.41777 | (1 0 1) |
| 4 | 10.61623 | 5.308117 | 0.188391 | 1.883907 | (1 0 6) |

| | | | | | |
|---|---|---|---|---|---|
| 5 | 12.27494 | 6.137468 | 0.162934 | 1.629336 | |
| 6 | 14.9603 | 7.480151 | 0.133687 | 1.336871 | |

**Table S2:** Calculation of Miller indices for DE-$WS_xO_y$.

| S.No. | 1/2r ($nm^{-1}$) | 1/r ($nm^{-1}$) | r (nm) | d-spacing ($A^o$) | (hkl) |
|---|---|---|---|---|---|
| 1 | 4.569131 | 2.284565256 | 0.43772004 | 4.377200421 | (1 0 0) |
| 2 | 6.432651 | 3.21632529 | 0.31091383 | 3.109138256 | (2 0 0) |
| 3 | 7.903356 | 3.951678075 | 0.25305705 | 2.53057051 | (1 0 1) |

## 7. BET Surface Area Analysis:

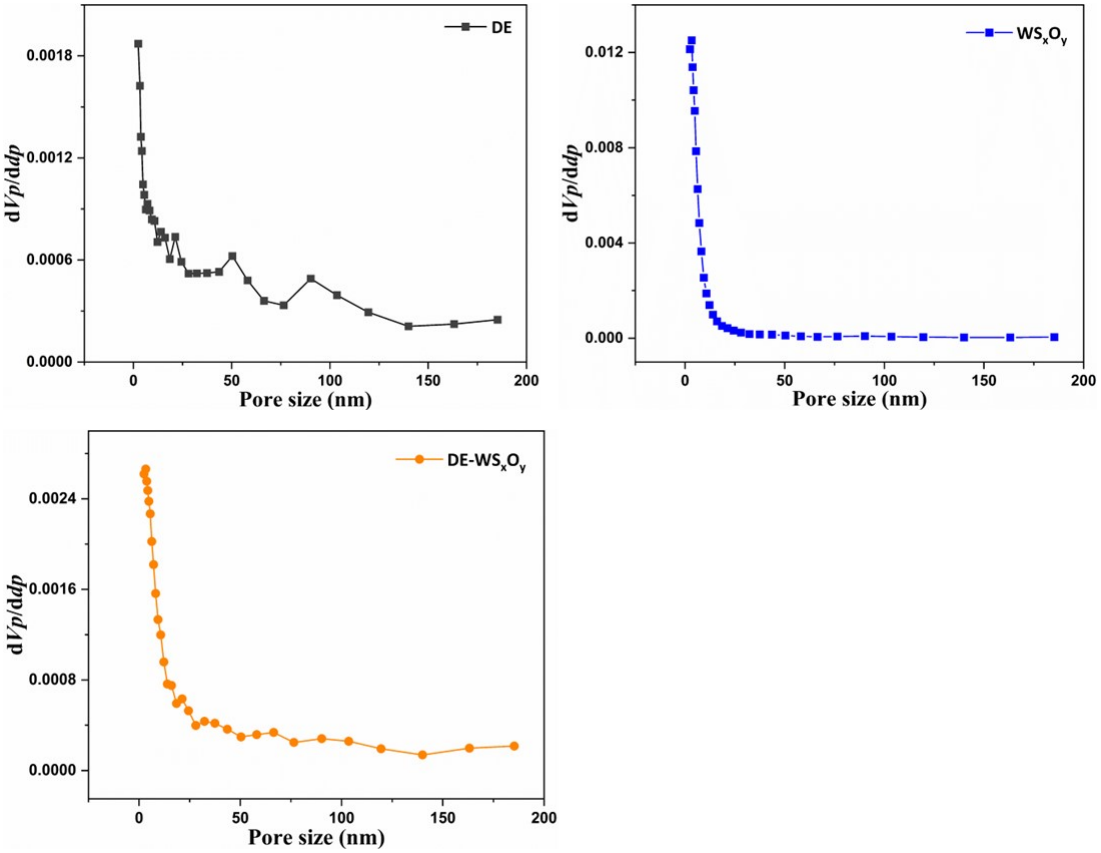


**Figure S8:** The pore size distribution plots for DE, $WS_xO_y$ and DE-$WS_xO_y$.

**Table S3:** Outline of the BET surface area parameters.

| Material | Surface area ($m^2/g$) | Pore diameter (nm) | Pore volume ($cm^3/g$) |
|---|---|---|---|

| | | | |
|---|---|---|---|
| DE | 26.169 | 12.983 | 0.084936 |
| $WS_xO_y$ | 100.15 | 4.1696 | 0.1044 |
| DE-$WS_xO_y$ | 24.383 | 11.952 | 0.072856 |

## 8. XPS Analysis:

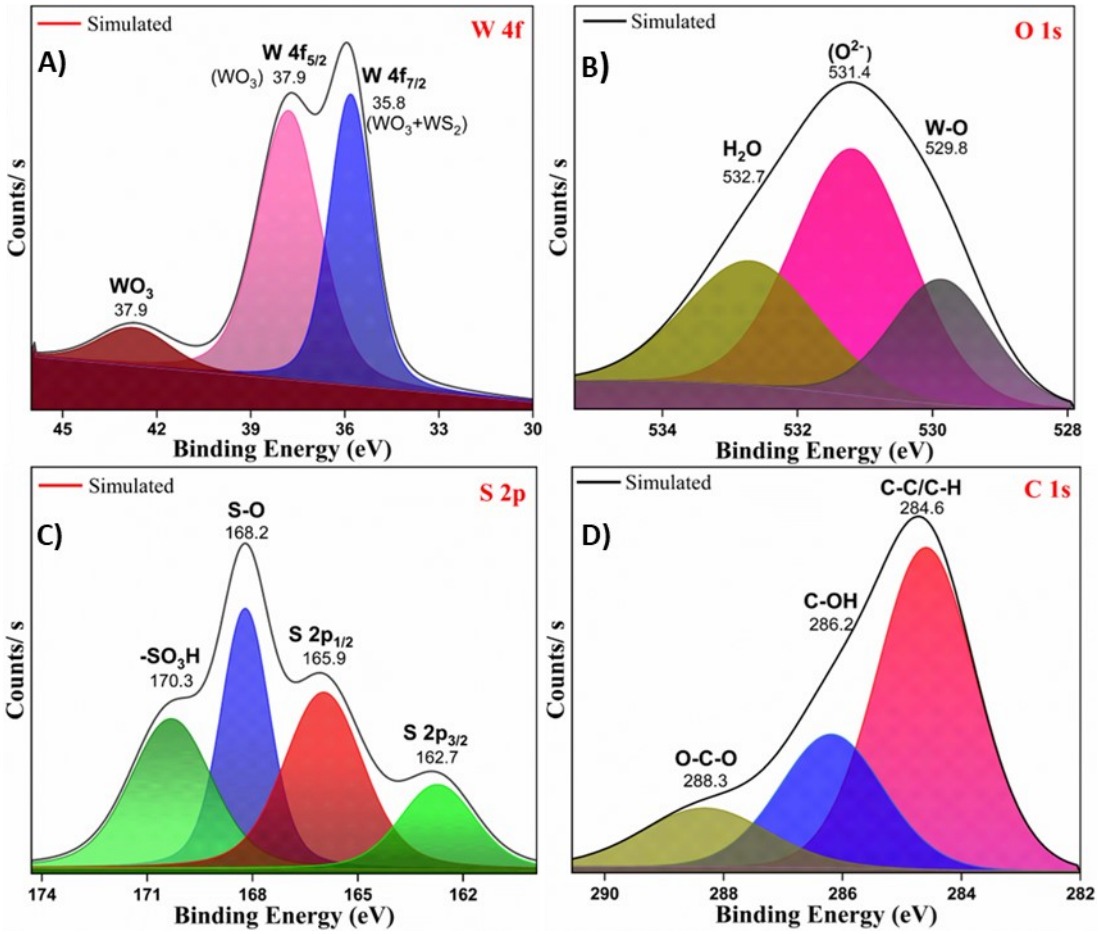


**Figure S9:** High-resolution spectra for W 4f, S 2p, O 1s and C 1s electrons of $WS_xO_y$.

**Table S4:** Elemental percentage of different atoms by XPS analysis.

| **Material** | **Atomic Composition (%)** | | | | |
|---|---|---|---|---|---|
| | C | Si | O | W | S |
| DE | 59.48 | 7.31 | 33.21 | - | - |
| $WS_xO_y$ | 50.77 | - | 44.37 | 0.13 | 1.5 |
| DE-$WS_xO_y$ | 45.6 | 6.87 | 46.69 | 0.12 | 0.42 |

## 9. Zeta potential Analysis:

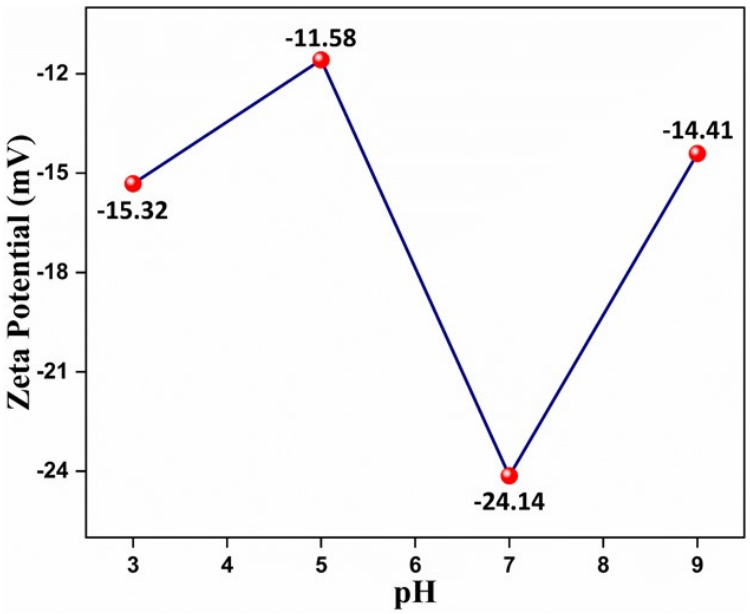


**Figure S10:** Zeta potential measurement of the DE-$WS_xO_y$ at different pH.

## 10. UV-Visible-DRS Analysis:

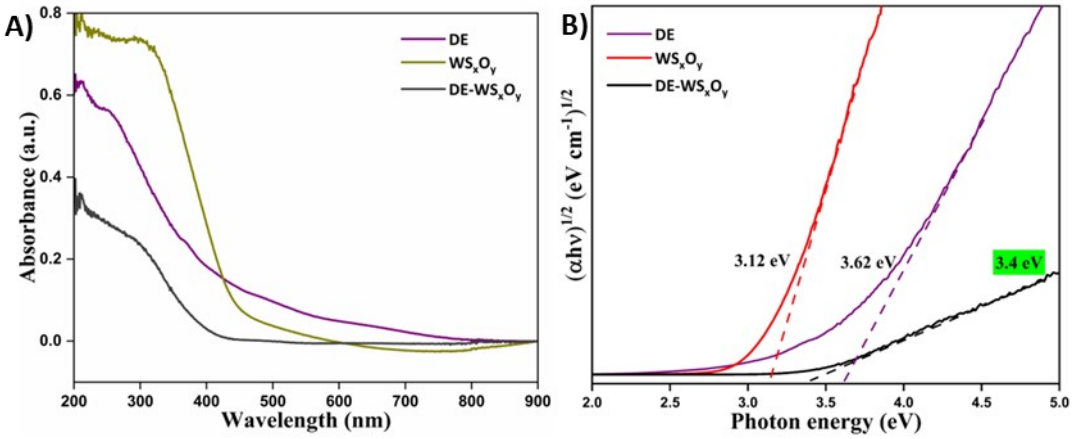


**Figure S11:** Energy band structure of DE, $WS_xO_y$ and DE-$WS_xO_y$. A) UV-Visible diffuse reflectance spectra, B) the corresponding tauc plot.

The band gap energies were calculated using the Tauc-equation:

$(\alpha h\upsilon)\ 1/m = k\ (h\upsilon - E_g)$ ……. (1)

Where, $E_g$ - The energy of optical band gap, k (constant) and m=1/2 in case of direct energy gap, m=2 in case of indirect energy gap.

**(αhν)$^{1/2}$** was plotted versus **hν** and the linear portion of the plot was extrapolated to the ordinate as shown in Figure S11B.

## 11. Results and Discussions:

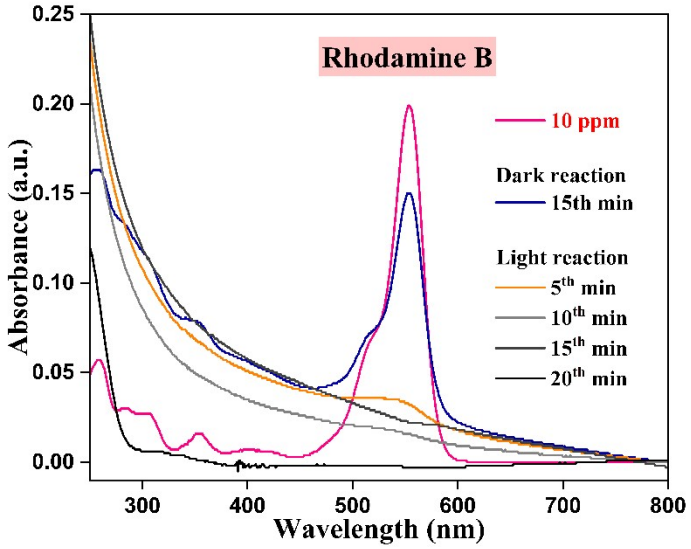


**Figure S12:** UV-Visible plot for the Decoloration of Rh B with DE- $WS_xO_y$ as catalyst.

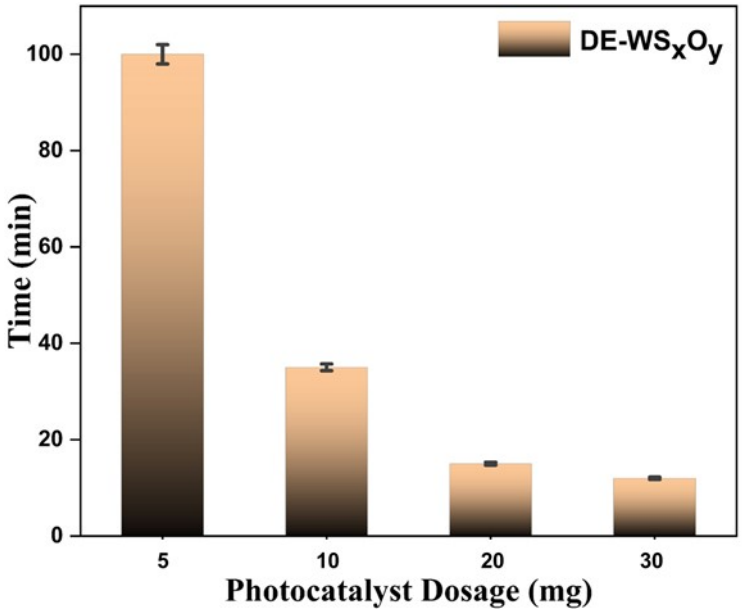


**Figure S13:** Effect of DE-$WS_xO_y$ photocatalyst dosage on photodegradation time.

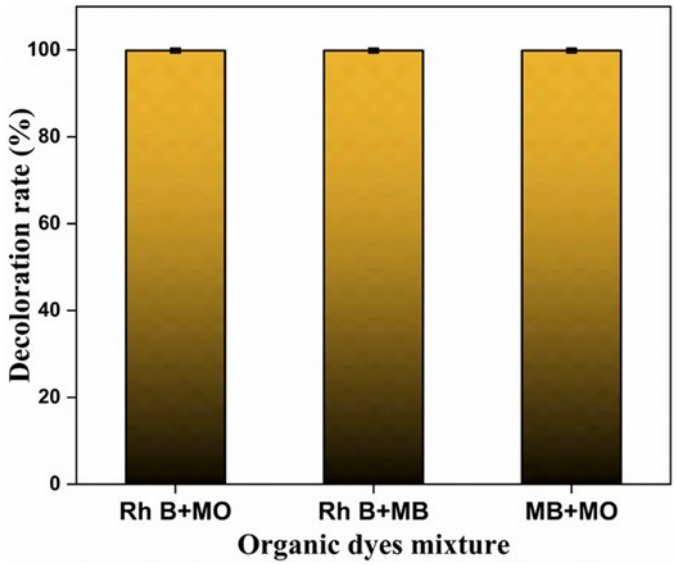


**Figure S14:** Photocatalytic activity for mixed dyes by DE-$WS_xO_y$.

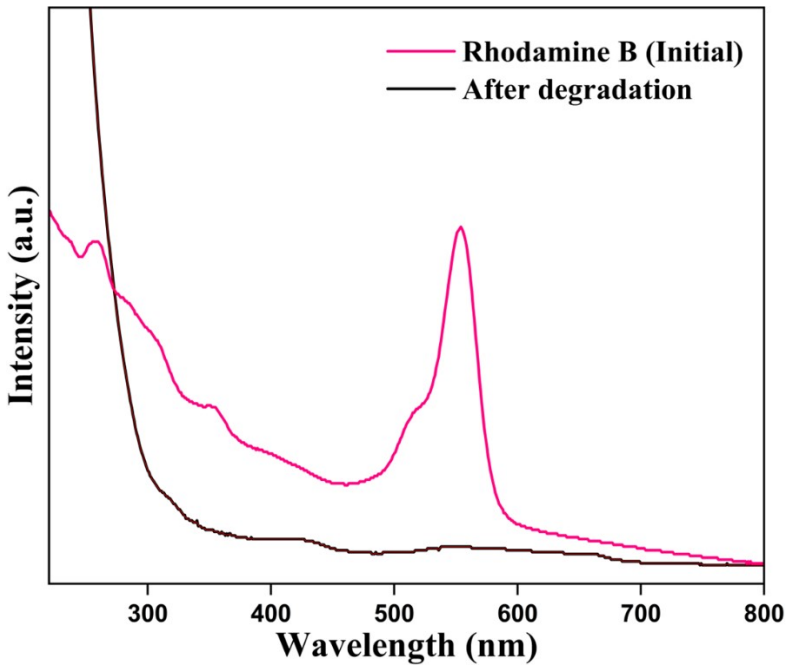


**Figure S15:** UV-Visible plot showing Photocatalytic activity for Rh B dye by DE-$WS_xO_y$ /PDMS cylindrical discs.

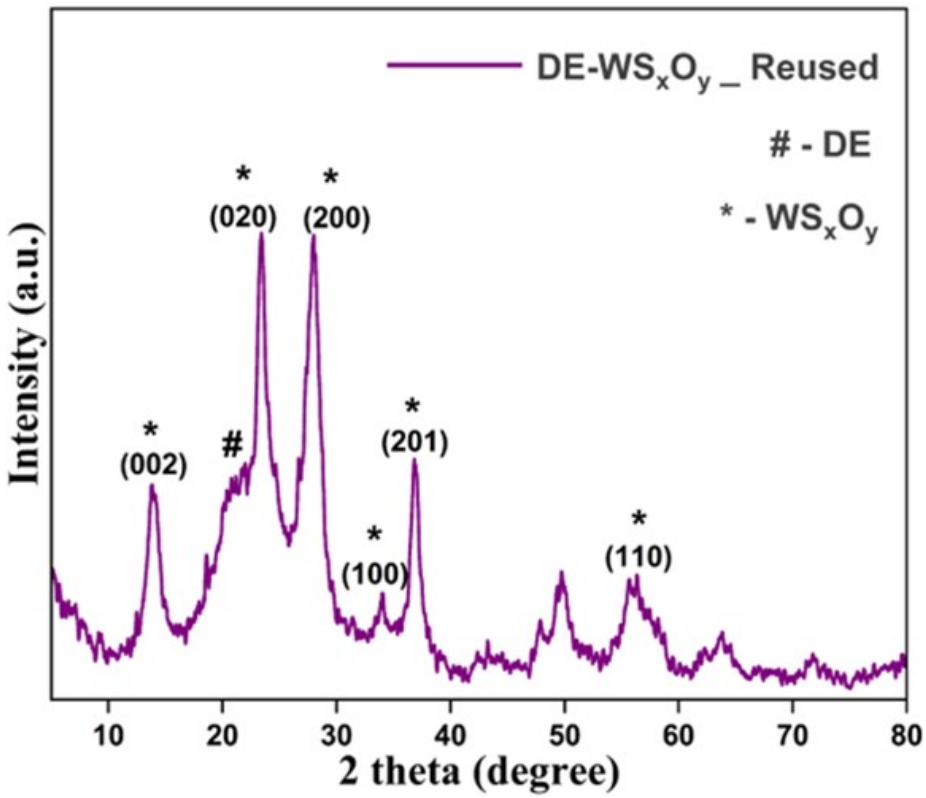


**Figure S16:** P-XRD analysis for phase structure analysis for reused DE-$WS_xO_y$ photocatalyst.

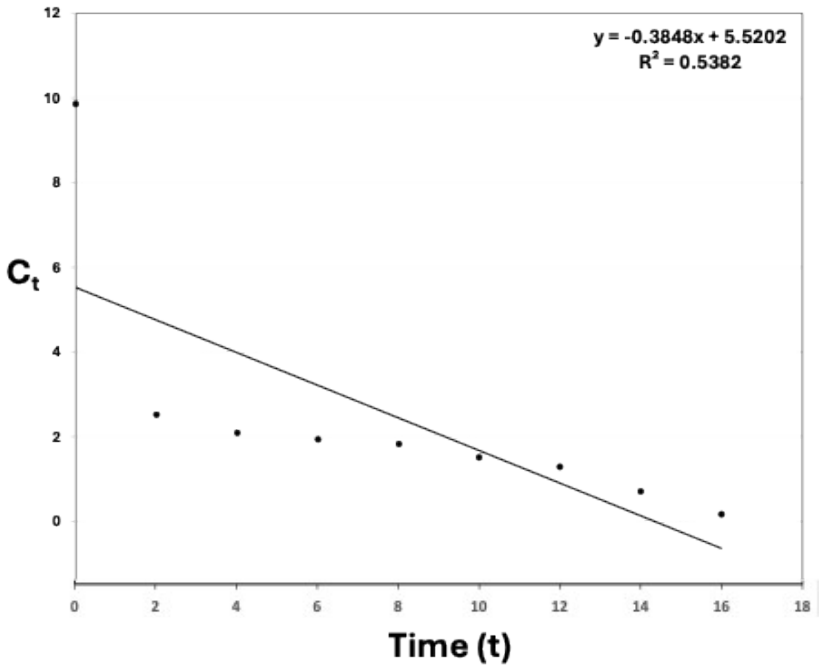


**Figure S17:** Zero-order kinetic model study for the photodegradation of rhodamine B by DE-$WS_xO_y$ catalyst.

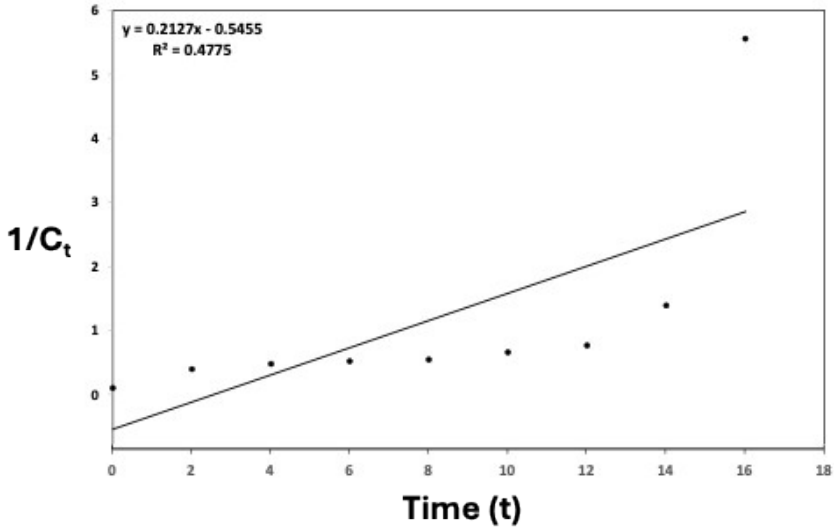


**Figure S18:** Second-order kinetic model study for the photodegradation of Rh B by DE-$WS_xO_y$ catalyst.

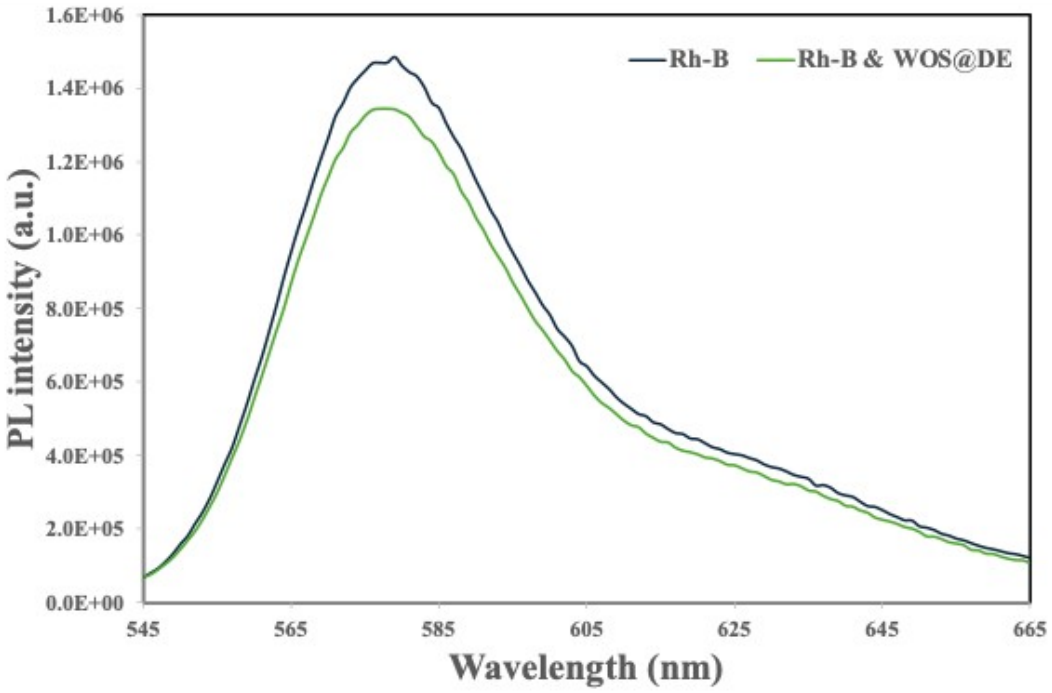


**Figure S19.** PL emission of Rhodamine B (1 mg $L^{-1}$) with and without DE-$WS_xO_y$ (2 mg) catalyst.

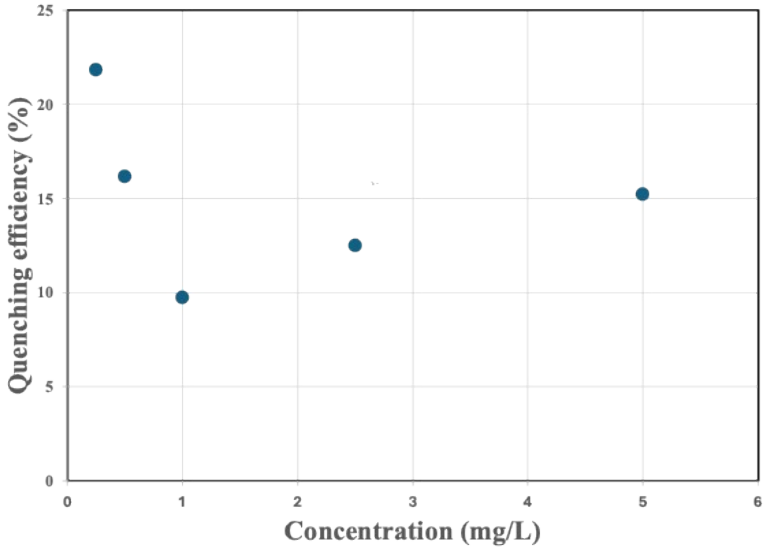


**Figure S20:** Quenching of Rhodamine B fluorescence by DE-$WS_xO_y$ catalyst as a function of dye concentration.

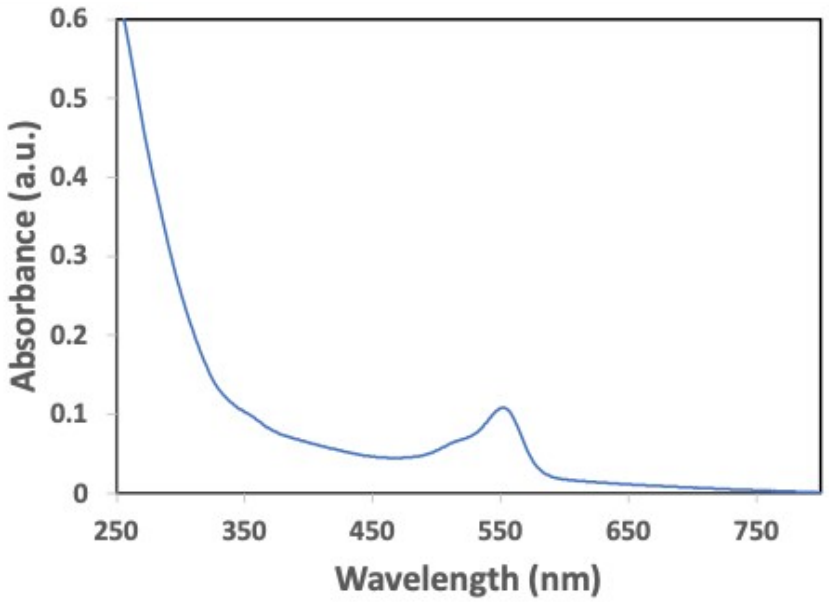


**Figure S21:** UV-visible plot showing sorption of Rh B on uncoated PDMS.